

## Unraveling the surface self-reconstruction of Fe-doped Ni-thiophosphate for efficient oxygen evolution reaction

Balakrishnan Kirubasankar<sup>a,b ‡</sup>, Yo Seob Won<sup>a ‡</sup>, Soo Ho Choi<sup>a,c</sup>, Jae Woo Kim<sup>a</sup>, Laud Anim Adofo<sup>b</sup>, Soo Min Kim<sup>b\*</sup> and Ki Kang Kim<sup>a,c\*</sup>

<sup>a</sup> B. Kirubasankar, Y. S. Won, S. H. Choi, J.W. Kim, K. K. Kim  
Department of Energy Science, Sungkyunkwan University, Suwon 16419, Republic of Korea.

<sup>b</sup> B. Kirubasankar, L. A. Adofo, S. M. Kim  
Department of Chemistry, Sookmyung Women's University, Seoul 140742, Republic of Korea.

<sup>c</sup> S. H. Choi, K. K. Kim  
Center for Integrated Nanostructure Physics (CINAP), Institute for Basic Science (IBS),  
Sungkyunkwan University, Suwon 16419, Republic of Korea.

\*E-mail: [soominkim@sookmyung.ac.kr](mailto:soominkim@sookmyung.ac.kr) and [kikangkim@skku.edu](mailto:kikangkim@skku.edu)

‡These authors contributed equally to this work.

### **This file includes:**

Experimental details

Discussion

Figure S1–S13

Tables S1–S3

## **Text S1 Experimental details**

### **1.1 Materials**

Nickel powder (99.99%, 203904), sulfur powder (99.99%, 213292), iodine (99.99%, 326143), Nafion (5 wt.% in a mixture of aliphatic alcohol and water, 663492), potassium hydroxide (>85.0%, 221473), and ruthenium oxide (99.90%, 208833) were purchased from Sigma-Aldrich. Iron powder (99.90%) and red phosphorus lump (99.99%) were acquired from Kojundo Chemical Laboratory. Platinum sheet counter electrode was procured from Bio-logic. Deionized (DI) water (18.2 M $\Omega$  at 25 °C) obtained from a Milli-Q System (Millipore, Billerica, MA) was used for all experiments. All the chemical reagents were used as received without further purification.

### **1.2 Synthesis of Ni<sub>x</sub>Fe<sub>1-x</sub>PS<sub>3</sub>**

Stoichiometric amounts of nickel, iron, phosphorus, and sulfur powders were sealed in quartz ampoules with internal pressure in the range of 10<sup>-5</sup>–10<sup>-6</sup> Torr. Iodine (2 mg cc<sup>-1</sup>) was incorporated into the quartz ampoule as a transport agent. The sealed tubes were then subjected to heat treatment in a two-zone horizontal tube furnace (hot zone at 750 °C and cold zone at 650 °C) for five days, as shown in Fig. S1, ESI.† The same procedure was followed for the preparation of NiPS<sub>3</sub> and FePS<sub>3</sub> without Fe and Ni, respectively.

### **1.3 Preparation of Ni<sub>x</sub>Fe<sub>1-x</sub>PS<sub>3</sub> nanosheet powder**

Ultrasonication was employed to exfoliate the bulk Ni<sub>x</sub>Fe<sub>1-x</sub>PS<sub>3</sub> into Ni<sub>x</sub>Fe<sub>1-x</sub>PS<sub>3</sub> nanosheets. Briefly, bulk Ni<sub>x</sub>Fe<sub>1-x</sub>PS<sub>3</sub> single crystals (200 mg) were added to ethanol (100 mL), followed by tip sonication (STH-750S, Jeio Tech) for 6 h. The resultant solution was centrifuged twice at 5000 rpm for 20 min. Then, 80% of the supernatant was filtrated and washed with ethanol. The filtered samples were dried overnight at 40 °C.

#### **1.4 Morphological and structural characterization**

XRD (Rigaku Smart Lab X-ray diffractometer) with Cu K $\alpha$  radiation and Raman spectroscopy (Xper-Ram 200, Nano Base) were used to characterize the crystal structures of the samples. To analyze the chemical state, ex-situ XPS (ESCALAB 250 XPS system) with Al K $\alpha$  radiation (1486.6 eV) was utilized. The surface morphology was characterized by scanning electron microscopy (SEM) (JSM-7100F, JEOL). The atomic structure and chemical elements were observed by a probe aberration-corrected 200 kV STEM (JEM-ARM200CF, JEOL) with a cold field emission source of 0.35eV energy resolution, equipped with energy-dispersive X-ray spectroscopy (EDS) detector of the silicon drift detector type. The high-angle annular dark-field scanning transmission electron microscopy (HAADF-STEM) images were acquired with a camera length of 8 cm and a collection angle of 68–280 mrad.

#### **1.5 In situ electrochemical Raman experiments**

Raman experiments were carried out with a confocal microscope Xper-Ram 200, Nano Base Raman system. The excitation wavelength was 532 nm from a DPSS laser, and a 40 microscope objective with a 0.60 numerical aperture was used for all Raman measurements. Wavenumber calibration was regularly verified by acquiring the Raman peak at 520 cm<sup>-1</sup> of a silicon crystal. In situ electrochemical Raman experiments were performed in a Raman electrochemical flow cell (Raman ECFC 3.5 cm<sup>2</sup>, 4.5 mL) with a Ni<sub>x</sub>Fe<sub>1-x</sub>PS<sub>3</sub> decorated glassy carbon electrode as the working electrode, a Pt wire as the counter electrode, and Ag/AgCl electrode as the reference electrode. A Biologic VSP potentiostat was used to control the potential. To avoid the influence of electro-oxidation, potential negative sweep is used to explore the oxygen evolution process, and the potential is from 0.1 V to 0.7 V (vs. Ag/AgCl).

#### **1.6 Electrodes preparation**

The electrocatalyst ink was prepared by blending 10 mg of the  $\text{Ni}_x\text{Fe}_{1-x}\text{PS}_3$  nanosheet powder with 30  $\mu\text{l}$  of Nafion (5 wt.%) and 0.97 ml of ethanol in an ultrasonic bath. Then, 50  $\mu\text{l}$  of homogeneously dispersed ink was drop-coated on the carbon cloth electrode (1 cm  $\times$  1 cm) with an active material mass loading of 0.5 mg  $\text{cm}^{-2}$ . For comparison, a  $\text{RuO}_2$  electrode was prepared (the catalyst loading amount was 0.7 mg  $\text{cm}^{-2}$ ).

### 1.7 Electrocatalytic Performance Tests

Linear sweep voltammetry (LSV) was carried out using Biologic VSP potentiostat at a scan rate of 2  $\text{mV s}^{-1}$  by sweeping the potential from 1.1 to 1.8 V vs. a reversible hydrogen electrode (RHE) in 1 M KOH with  $iR$  correction (compensation 85%). A three-electrode system consisting of as-prepared  $\text{Ni}_x\text{Fe}_{1-x}\text{PS}_3$  ink coated on carbon cloth as the working electrode, saturated calomel electrode (SCE) as the reference electrode, and Pt sheet as the counter electrode. The measured potential vs. SCE was converted to an RHE scale using  $E_{\text{RHE}} = E_{\text{SCE}} + 0.241 \text{ V} + 0.059 \text{ pH}$  in 1 M KOH at a pH of 14. Before the test, the electrolyte was purged with  $\text{O}_2$  gas for 0.5 h and the electrocatalyst was activated by conducting CV tests at a scan rate of 100  $\text{mV s}^{-1}$ . All the tests were performed at room temperature. EIS measurements were performed at an overpotential of 280 mV in the frequency range from 100 kHz to 10 mHz with an amplitude of 20 mV. Faradaic efficiency was calculated via water displacement method. Faradaic efficiency is defined as the ratio of the experimentally detected quantity of  $\text{O}_2$  to the theoretically calculated quantity of  $\text{O}_2$ . The theoretically calculated amount of oxygen was calculated using the following equation from Faraday's law.

The theoretical amount of  $\text{O}_2$  gas was calculated from Faraday's law

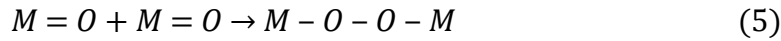
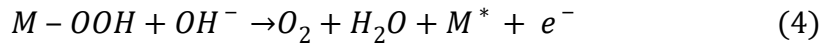
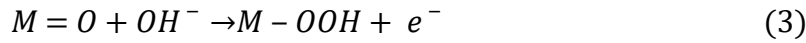
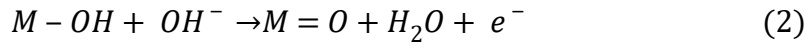
$$n_{\text{O}_2} = \frac{Q}{n \times F} = \frac{I \times t}{n \times F} \quad (1)$$

where  $m$  is the theoretically calculated amount of  $O_2$ ,  $Q$  is the amount of applied charge,  $n$  is the number of electrons participating in the OER reaction (4 electrons),  $F$  is the Faraday constant (96485.3 s A mol<sup>-1</sup>),  $I$  is the applied current, and  $t$  is the reaction time.

$$\text{Faradaic efficiency} = \frac{n_{O_2} (\text{measured})}{n_{O_2} (\text{theoretical})} \quad (2)$$

## Text S2 Single- and dual-site OER mechanisms

The typical OER reactions are as follows: <sup>1</sup>



where  $M^*$  denotes the metal cation (Ni/Fe) of  $Ni_{0.8}Fe_{0.2}PS_3$ .  $M-OH$ ,  $M-OOH$ , and  $M=O$  are surface bound intermediates. During OER in single-site (reactions 1–4), Ni/Fe is adsorbed/desorbed by  $OH^-$  ions in an alkaline electrolyte and forms  $NiOOH$  and  $FeOOH$  species on the surface. These metal (oxy)hydroxide ions can further combine with  $OH^-$  to generate  $O_2$ .<sup>2,3</sup> In the dual-site OER mechanism (reactions 1, 2, 5, and 6), both Ni and Fe species were involved in the electron transfer process and formed O–O bonds via two  $M=O$  units. This  $M-O-O-M$  species can generate  $O_2$ .<sup>4</sup> The dual-site mechanism in  $Ni_{0.8}Fe_{0.2}PS_3$  probably enhances the OER kinetics.

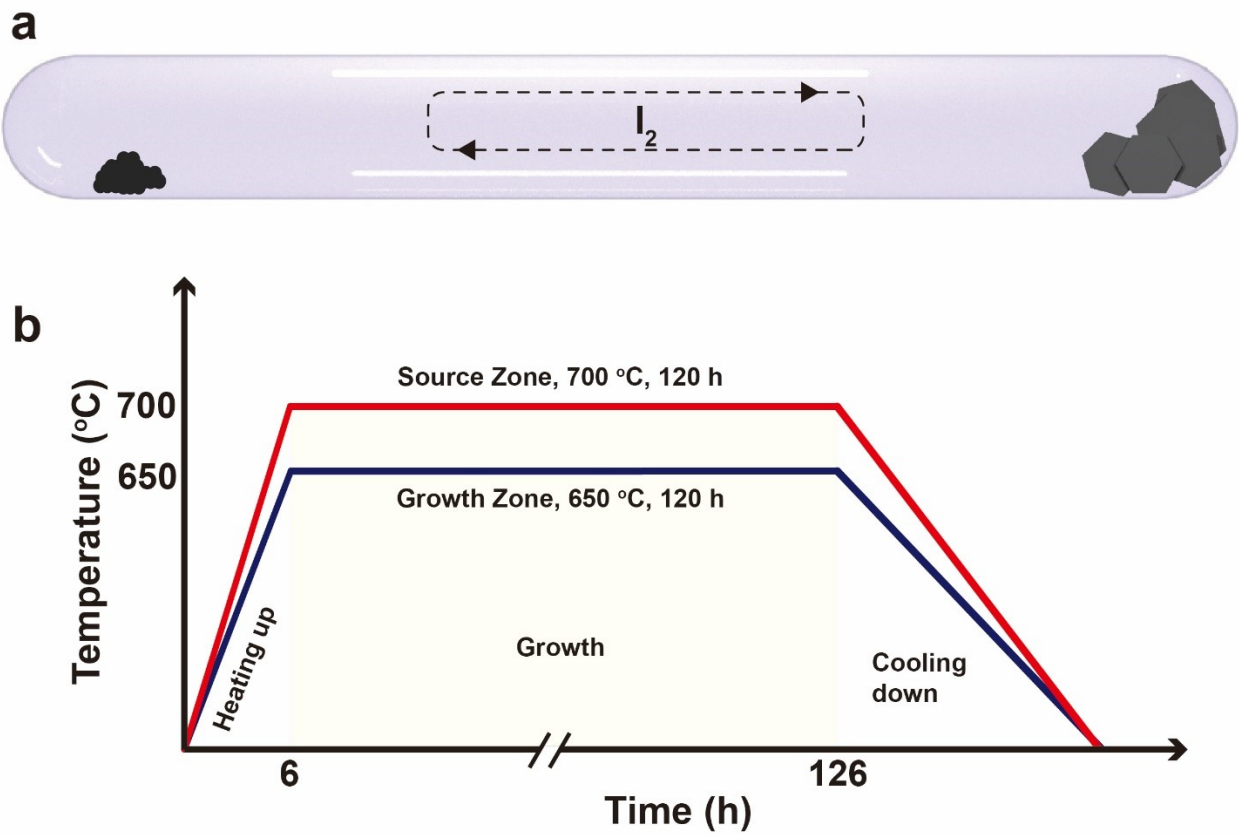


**Figure S1.** (a) Schematic of the CVT synthesis process using iodine as the transport agent. (b) Temperature profile for CVT process.

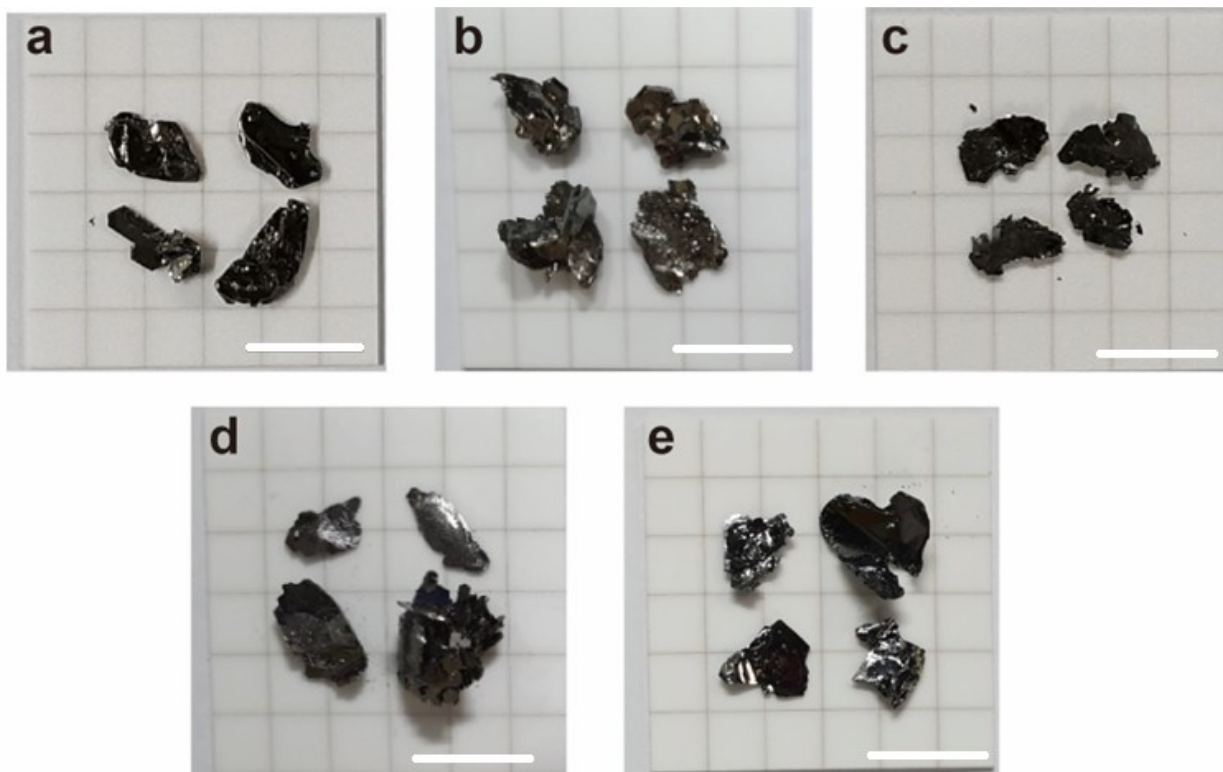


**Figure S2.** Photographs of (a)  $\text{NiPS}_3$ , (b)  $\text{Ni}_{0.9}\text{Fe}_{0.1}\text{PS}_3$ , (c)  $\text{Ni}_{0.8}\text{Fe}_{0.2}\text{PS}_3$ , (d)  $\text{Ni}_{0.7}\text{Fe}_{0.3}\text{PS}_3$ , and (e)  $\text{FePS}_3$  single crystals. Scale bar equals 1 cm.

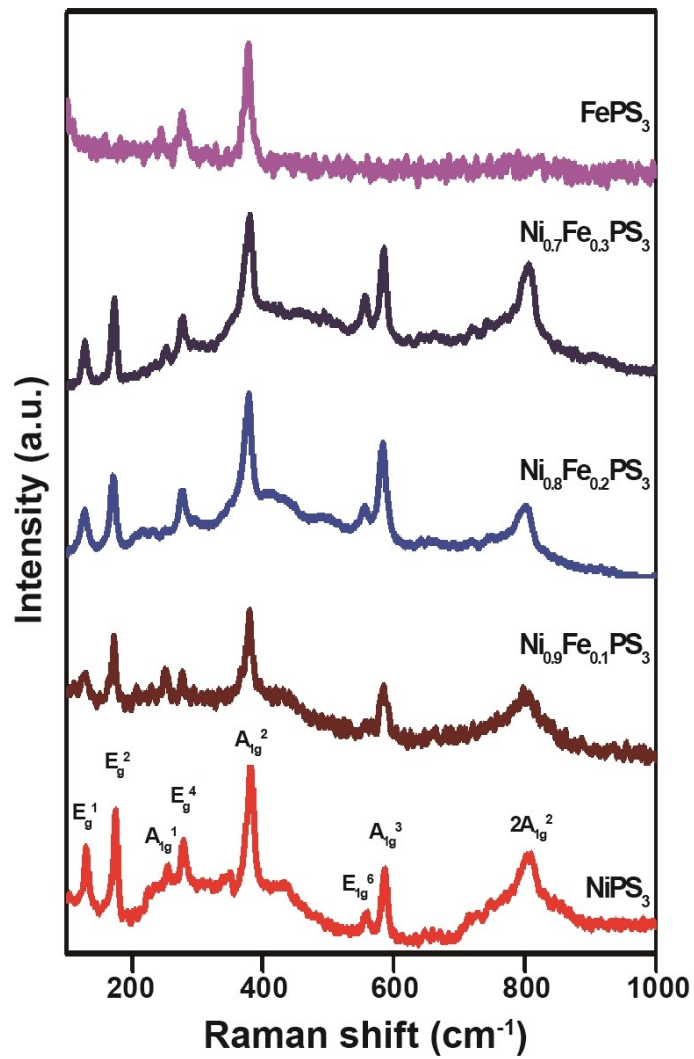


**Figure S3.** Raman spectra of  $\text{Ni}_x\text{Fe}_{1-x}\text{PS}_3$  ( $x=1, 0.9, 0.8, 0.7$ , and  $0$ ).

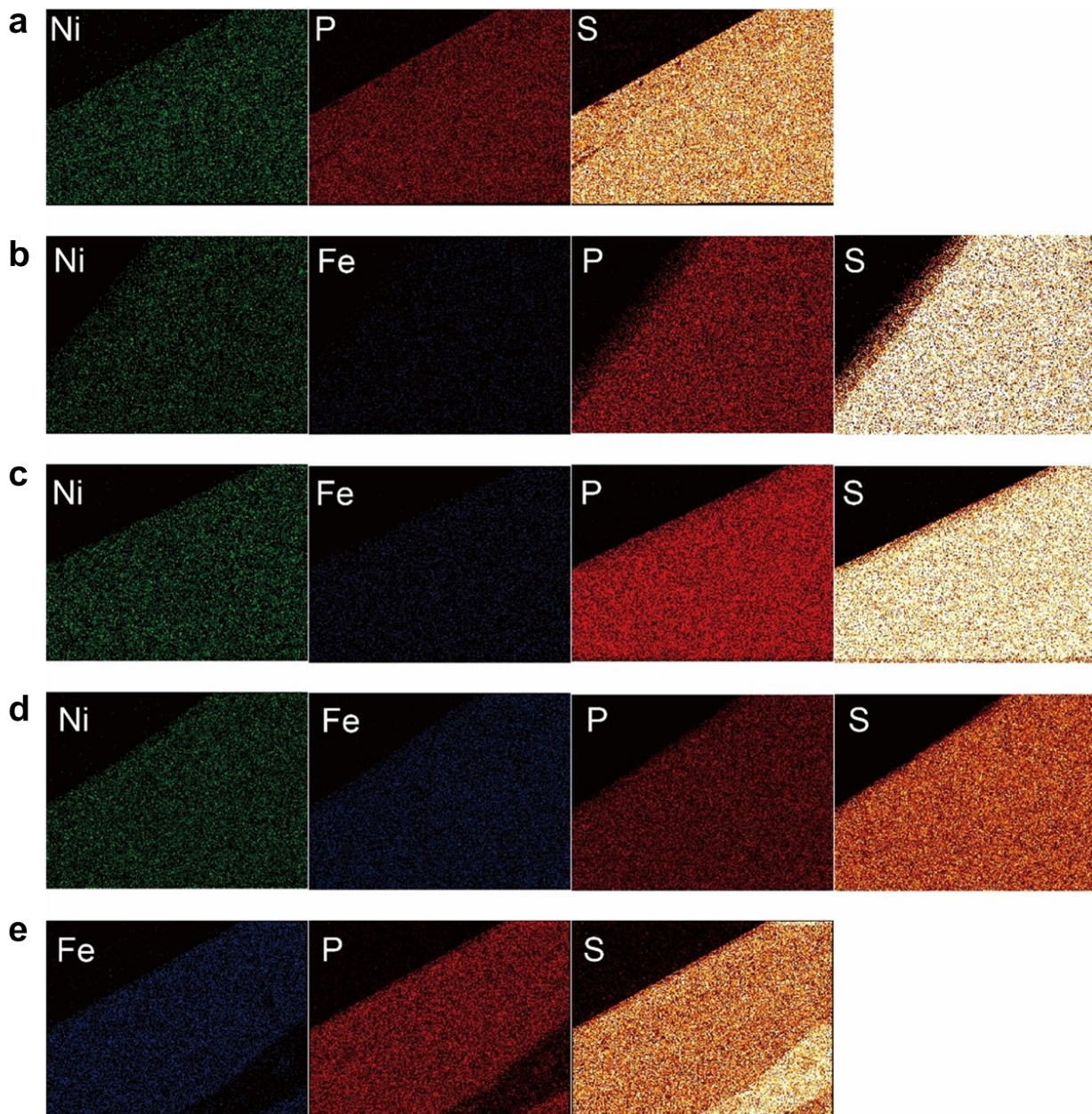


**Figure S4.** EDS (for Ni, Fe, P, and S) mapping images of (a)  $\text{NiPS}_3$ , (b)  $\text{Ni}_{0.9}\text{Fe}_{0.1}\text{PS}_3$ , (c)  $\text{Ni}_{0.8}\text{Fe}_{0.2}\text{PS}_3$ , (d)  $\text{Ni}_{0.7}\text{Fe}_{0.3}\text{PS}_3$ , and (e)  $\text{FePS}_3$  single crystals observed via SEM.

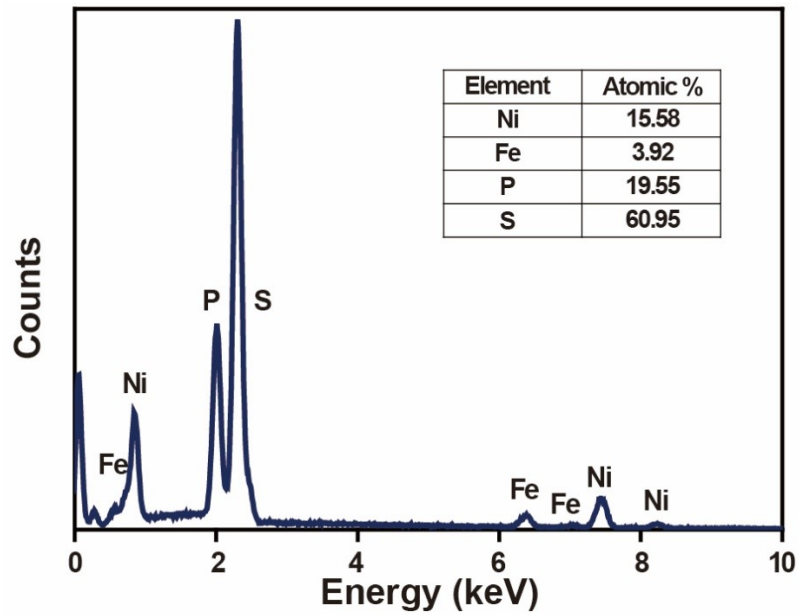


**Figure S5.** EDS spectrum of  $\text{Ni}_{0.8}\text{Fe}_{0.2}\text{PS}_3$  with atomic % of each element.



**Figure S6.** Photograph of oxygen gas collection. Oxygen gas is generated during chronopotentiometry at  $20 \text{ mA cm}^{-2}$ .

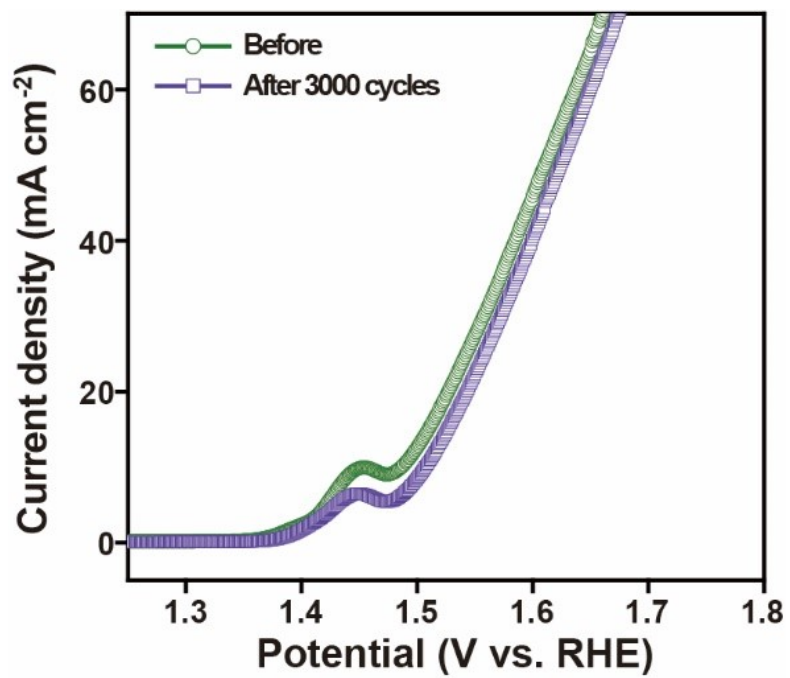


**Figure S7.** LSV curves before and after 3000 cycles of  $\text{Ni}_{0.8}\text{Fe}_{0.2}\text{PS}_3$ .

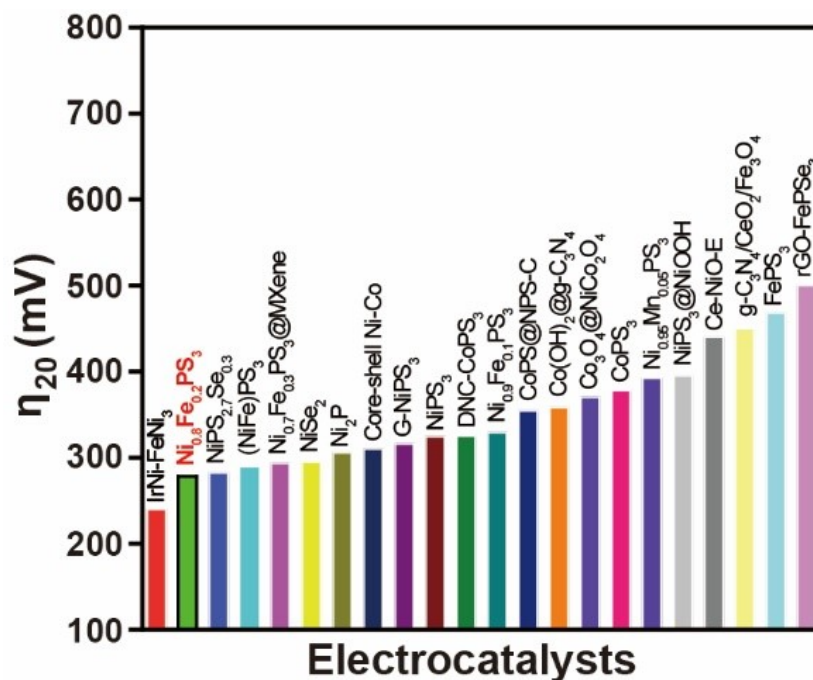


**Figure S8.** Comparison of overpotentials at 20 mA cm<sup>-2</sup> with other first-row 3d transition metal (Ni, Co, and Fe) thiophosphate electrocatalysts.

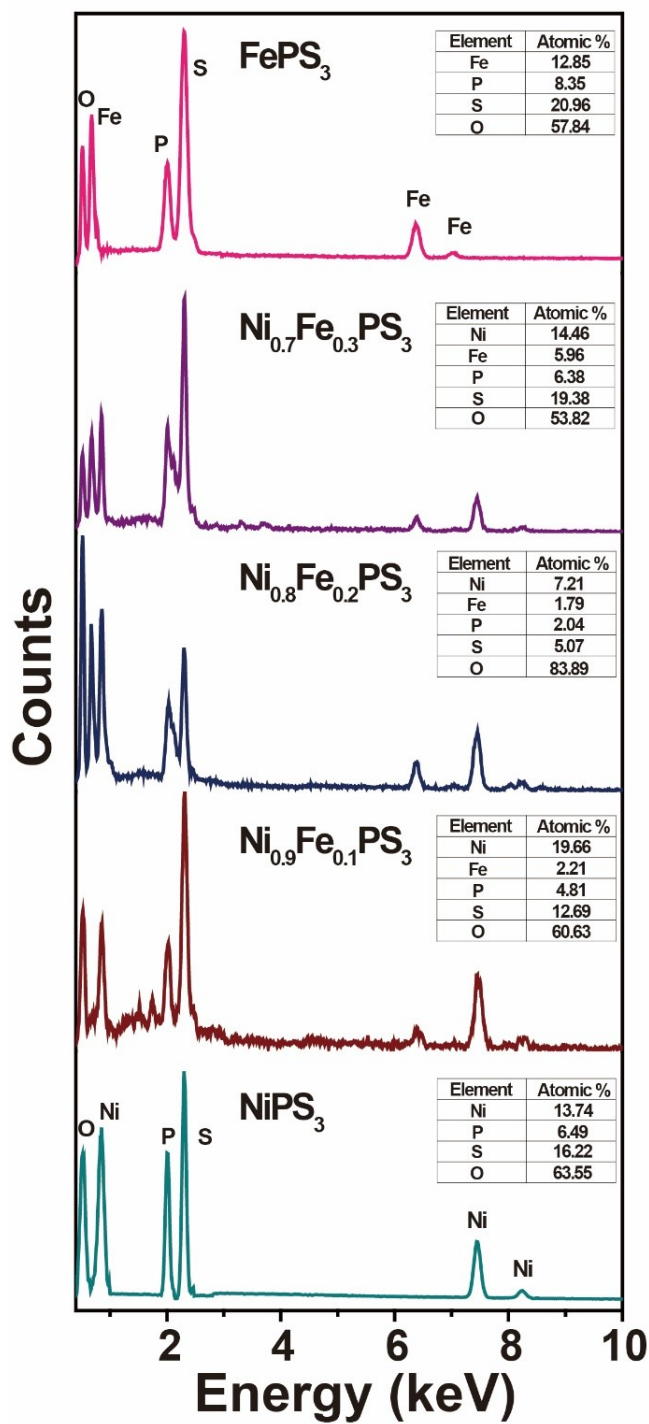


**Figure S9.** EDS spectral profiles of all catalysts with different Fe/Ni ratio after OER. The atomic percentage of O increase, while P and S decrease for all Ni<sub>x</sub>Fe<sub>1-x</sub>PS<sub>3</sub>.

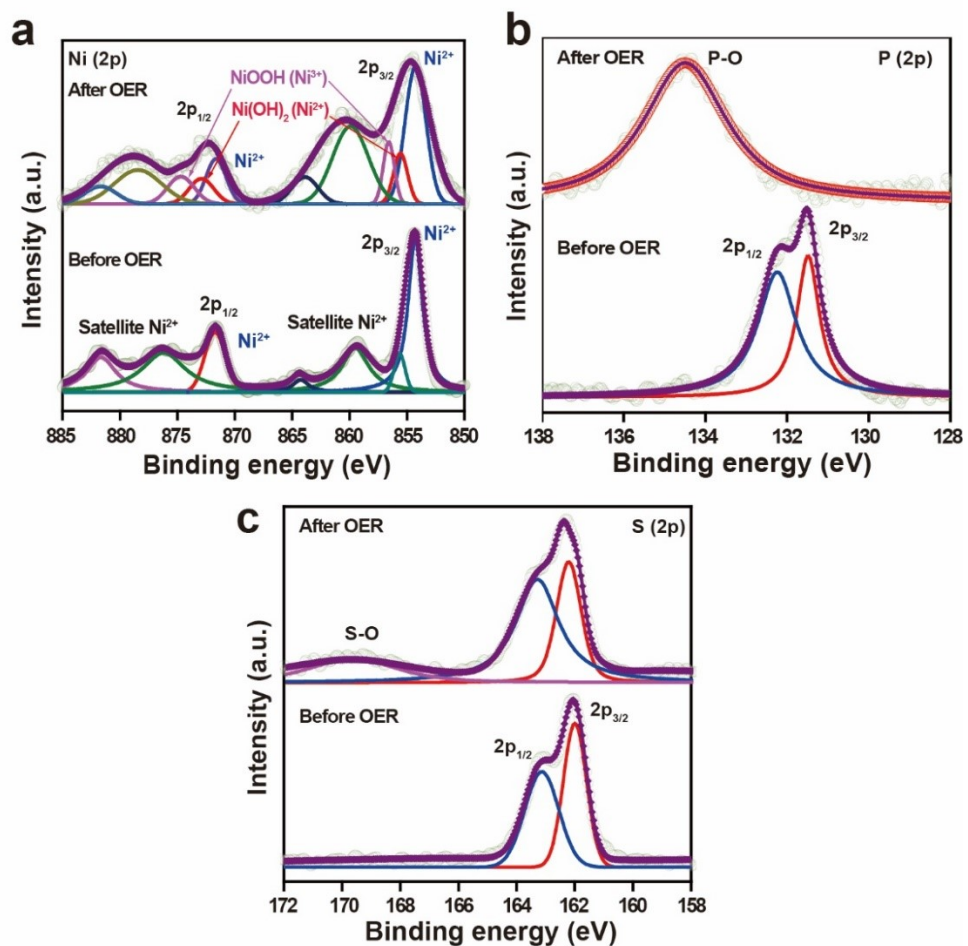


**Figure S10.** XPS core level spectra of (a) Ni (2p), (b) P (2p), and (c) S (2p) before (bottom) and after OER (top). The development of P–O and S–O peaks are clearly observed.

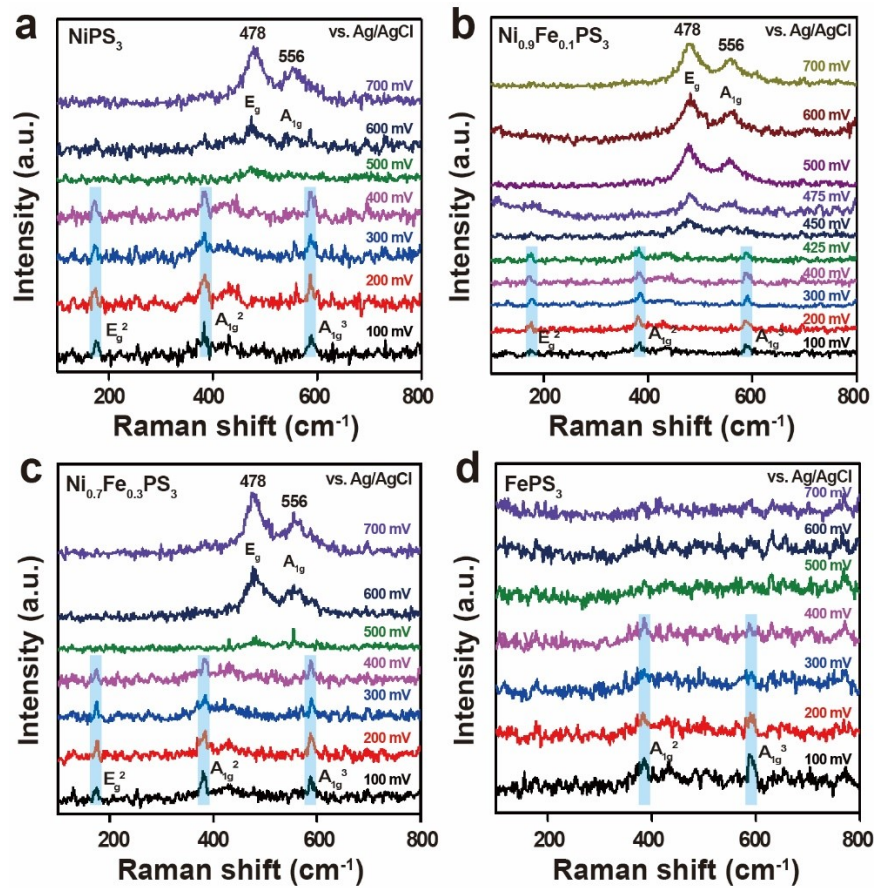


**Figure S11.** *In-situ* Raman spectroscopy analysis to investigate the effect of Fe-doping in NiPS<sub>3</sub> for (a) NiPS<sub>3</sub>, (b) Ni<sub>0.9</sub>Fe<sub>0.1</sub>PS<sub>3</sub>, (c) Ni<sub>0.7</sub>Fe<sub>0.3</sub>PS<sub>3</sub>, and (d) FePS<sub>3</sub> during OER.

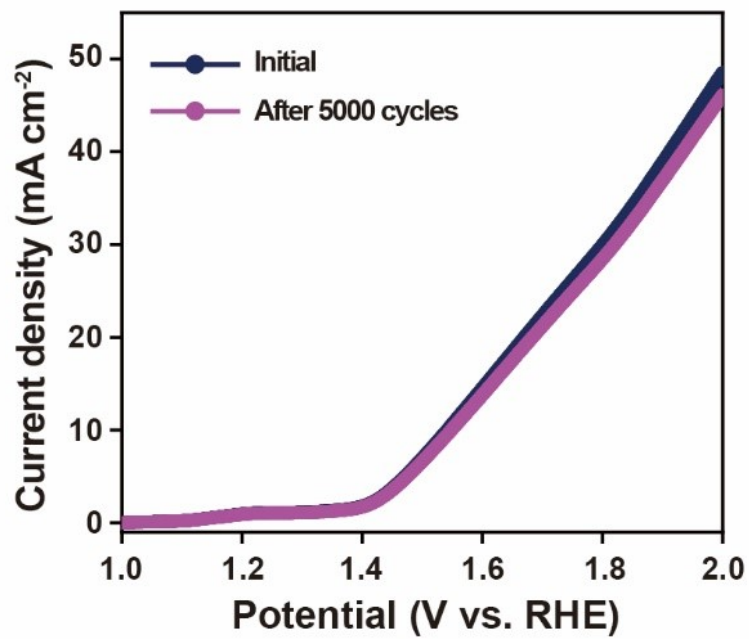


**Figure S12.** LSV curves before and after 5000 cycles for Ni<sub>0.8</sub>Fe<sub>0.2</sub>PS<sub>3</sub>||Pt/C.

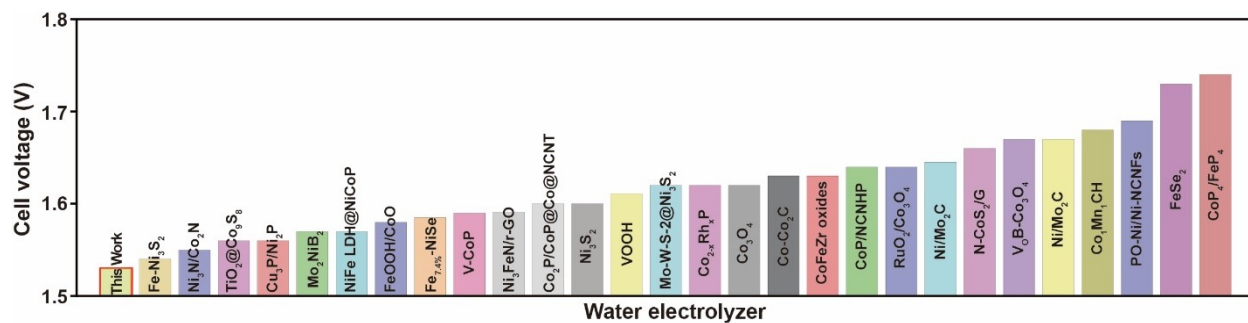


**Figure S13.** Comparison of the full-cell water splitting cell voltage at  $10 \text{ mA cm}^{-2}$  with different OER electrocatalysts including transition metal sulfides, phosphides, and carbides under alkaline medium.

**Table S1** Summary of EIS parameters calculated for  $\text{Ni}_x\text{Fe}_{1-x}\text{PS}_3$  ( $x=1, 0.9, 0.8, 0.7,$  and  $0$ ) electrodes.

Catalyst	$R_s$ ( $\Omega$ )	$R_{ct}$ ( $\Omega$ )	$C_{dl}$ ( $\text{mF cm}^{-2}$ )
$\text{NiPS}_3$	0.91	9.8	35.97
$\text{Ni}_{0.9}\text{Fe}_{0.1}\text{PS}_3$	1.01	7.5	29.14
$\text{Ni}_{0.8}\text{Fe}_{0.2}\text{PS}_3$	1.39	2.8	13.56
$\text{Ni}_{0.7}\text{Fe}_{0.3}\text{PS}_3$	0.89	4.1	21.27
$\text{FePS}_3$	1.31	41.0	64.01
$\text{RuO}_2$	1.35	18.7	48.19

**Table S2** Comparison of the OER activity of Ni<sub>0.8</sub>Fe<sub>0.2</sub>PS<sub>3</sub> and thiophosphate-based catalysts at constant current density of 20 mA cm<sup>-2</sup> in 1 M KOH.

Catalyst	Tafel slope (mV dec <sup>-1</sup> )	$\eta_{20}$ (mV)	Reference
<b>Ni<sub>0.8</sub>Fe<sub>0.2</sub>PS<sub>3</sub></b>	<b>52</b>	<b>278</b>	<b>Present study</b>
Ni <sub>0.7</sub> Fe <sub>0.3</sub> PS <sub>3</sub> @MXene	36.5	293	<i>Adv. Energy Mater.</i> <b>2018</b> , <i>14</i> , 1801127
Ni <sub>0.9</sub> Fe <sub>0.1</sub> PS <sub>3</sub>	56	329	<i>ACS Catal.</i> <b>2017</b> , <i>7</i> , 8549
(NiFe)PS <sub>3</sub>	41.7	289	<i>J. Power Source</i> <b>2018</b> , <i>403</i> , 90
NiPS <sub>2.7</sub> Se <sub>0.3</sub> NSs	76	282	<i>Adv. Funct. Mater.</i> <b>2021</b> , <i>31</i> , 2100618
G-NiPS <sub>3</sub>	42.6	316	<i>ACS Nano</i> <b>2018</b> , <i>12</i> , <i>6</i> , 5297
NiPS <sub>3</sub>	43	324	<i>Nanoscale</i> <b>2018</b> , <i>10</i> , 4890
NiPS <sub>3</sub> @NiOOH	80	395	<i>ACS Catal.</i> <b>2017</b> , <i>7</i> , 229
DNC-CoPS <sub>3</sub>	51.8	325	<i>Intl. J. Hydrogen Energy</i> <b>2022</b> , <i>47</i> , 197
CoPS <sub>3</sub>	95	378	<i>ACS Appl. Mater. Interfaces</i> , <b>2021</b> , <i>13</i> , 23638
Ni <sub>0.95</sub> Mn <sub>0.05</sub> PS <sub>3</sub>	138	392	<i>J. Alloys Comp.</i> <b>2018</b> , <i>769</i> , 532
FePS <sub>3</sub>	58	468	<i>Chem. Comm.</i> <b>2018</b> , <i>54</i> , 4481
rGO-FePSe <sub>3</sub>	117	500	<i>ACS Appl. Energy Mater.</i> <b>2018</b> , <i>1</i> , 220
CoPS@NPS-C	98	354	<i>J. Mater. Chem. A</i> , <b>2018</b> , <i>6</i> , 10433
NiSe <sub>2</sub>	53.4	295	<i>Small</i> <b>2017</b> , <i>13</i> , 1701487
Ni <sub>2</sub> P NPs	47	305	<i>Energy Environ. Sci.</i> , <b>2015</b> , <i>8</i> , 2347
IrNi-FeNi <sub>3</sub> HNSs	36.01	240	<i>Appl. Catal. B</i> , <b>2021</b> , <i>286</i> , 119881
Core-Shell Ni-Co NW	43.6	310	<i>Adv. Energy Mater.</i> , <b>2017</b> , <i>7</i> , 1601492
Co(OH) <sub>2</sub> @g-C <sub>3</sub> N <sub>4</sub>	59	358	<i>J. Mater. Chem. A</i> , <b>2016</b> , <i>4</i> , 12940
Co <sub>3</sub> O <sub>4</sub> /NiCo <sub>2</sub> O <sub>4</sub>	88	370	<i>J. Am. Chem. Soc.</i> <b>2015</b> , <i>137</i> , 5590
Ce-NiO-E	118.7	440	<i>Adv. Funct. Mater.</i> , <b>2018</b> , <i>28</i> , 1706056
g-C <sub>3</sub> N <sub>4</sub> /CeO <sub>2</sub> /Fe <sub>3</sub> O <sub>4</sub>	74	450	<i>ChemCatChem</i> , <b>2018</b> , <i>10</i> , 5587

\*NS: nanosheets; G: Graphene; DNC: nitrogen-doped carbon; rGO: reduced graphene oxide; NPS-C: nitrogen, phosphorus, and sulfur tri-doped porous carbon; NPs: nanoparticles; HNSs: hybrid nanosheets; and NW: nanowires.

**Table S3** Overpotentials of various OER catalysts for full-cell water splitting in 1 M KOH.

OER catalyst  Pt/C	$\eta$ (mV) at 10 mA cm <sup>-2</sup>	Reference
<b>Ni<sub>0.8</sub>Fe<sub>0.2</sub>PS<sub>3</sub></b>	<b>1.53</b>	<b>Present study</b>
Fe-Ni <sub>3</sub> S <sub>2</sub>	1.54	<i>ACS Catal.</i> , <b>2018</b> , 8, 5431
Ni <sub>3</sub> N/Co <sub>2</sub> N	1.55	<i>J. Mater. Chem. A</i> , <b>2021</b> , 9, 10260
TiO <sub>2</sub> @Co <sub>9</sub> S <sub>8</sub>	1.56	<i>Adv. Sci.</i> , <b>2018</b> , 5, 1700772
Cu <sub>3</sub> P/Ni <sub>2</sub> P	1.56	<i>Chem. Eng. J.</i> , <b>2022</b> , 448, 137706
Mo <sub>2</sub> NiB <sub>2</sub>	1.57	<i>Small</i> <b>2022</b> , 18, 2104303
NiFe LDH@NiCoP	1.57	<i>Adv. Funct. Mater.</i> , <b>2018</b> , 28, 1706847
FeOOH/CoO	1.58	<i>Chem. Eur. J.</i> , <b>2020</b> , 26, 4120
Fe <sub>7.4%</sub> -NiSe	1.58	<i>J. Mater. Chem. A</i> , <b>2019</b> , 7, 2233
V-CoP	1.59	<i>Adv. Energy Mater.</i> , <b>2021</b> , 11, 2101758
Ni <sub>0.75</sub> Fe <sub>0.125</sub> V <sub>0.125</sub> - LDHs/NF	1.59	<i>Small</i> , <b>2018</b> , 14, 1703257
Ni <sub>3</sub> FeN (111)/r-GO	1.60	<i>ACS Nano</i> , <b>2018</b> , 12, 245
Co <sub>2</sub> P/CoP@Co@NCNT	1.60	<i>Chem. Eng. J.</i> , <b>2022</b> , 430, 132877
VOOH	1.62	<i>Angew. Chem. Int. Ed.</i> , <b>2017</b> , 56, 573
Mo-W-S-2@Ni <sub>3</sub> S <sub>2</sub>	1.62	<i>ACS Appl. Mater. Interfaces</i> , <b>2017</b> , 9, 26066
Co <sub>2-x</sub> Rh <sub>x</sub> P	1.62	<i>ChemCatChem</i> , <b>2021</b> , 13, 4111
Co <sub>3</sub> O <sub>4</sub> microtube arrays	1.63	<i>Angew. Chem. Int. Ed.</i> , <b>2017</b> , 56, 1324
Co-Co <sub>2</sub> C	1.63	<i>Appl. Catal. B</i> , <b>2021</b> , 296, 120334
CoFeZr oxides	1.64	<i>Adv. Mater.</i> , <b>2019</b> , 31, 1901439
CoP/NCNHP	1.64	<i>J. Am. Chem. Soc.</i> , <b>2018</b> , 140, 2610
RuO <sub>2</sub> /Co <sub>3</sub> O <sub>4</sub>	1.64	<i>Appl. Catal. B</i> , <b>2020</b> , 263, 118324
Ni/Mo <sub>2</sub> C	1.66	<i>Chem. Sci.</i> , <b>2017</b> , 8, 968
N-CoS <sub>2</sub> NP on N,S-G	1.67	<i>ChemSusChem</i> , <b>2020</b> , 13, 5112
V <sub>O</sub> B-Co <sub>3</sub> O <sub>4</sub>	1.67	<i>Chem. Eng. J.</i> , <b>2021</b> , 404, 126474
Co <sub>1</sub> Mn <sub>1</sub> CH	1.68	<i>J. Am. Chem. Soc.</i> , <b>2017</b> , 139, 8320
PO-Ni/Ni-N-CNFs	1.69	<i>Nano Energy</i> , <b>2018</b> , 51, 286
FeSe <sub>2</sub>	1.73	<i>Angew. Chem. Int. Ed.</i> , <b>2017</b> , 56, 10506
CoP <sub>4</sub> /FeP <sub>4</sub>	1.74	<i>Int. J. Hydrogen Energy</i> , <b>2022</b> , 47, 23230

\*rGO: reduced graphene oxide; LDH: layered double hydroxide; NF: nickel foam; NCNT: nitrogen-doped carbon nanotube; NCNHP: nitrogen-doped carbon nanotube hollow polyhedron; N,S-G: nitrogen-sulfur co-doped graphene; V<sub>O</sub>: oxygen vacancy; CH: carbonate hydroxide; PO: partially oxidized; and CNFs: carbon nanofibers.

## References

- 1 N. Zhang, X. Feng, D. Rao, X. Deng, L. Cai, B. Qiu, R. Long, Y. Xiong, Y. Lu and Y. Chai, *Nat. Commun.*, 2020, **11**, 1–11.
- 2 X. Yu, Z.-Y. Yu, X.-L. Zhang, Y.-R. Zheng, Y. Duan, Q. Gao, R. Wu, B. Sun, M.-R. Gao, G. Wang and S.-H. Yu, *J. Am. Chem. Soc.*, 2019, **141**, 7537–7543.
- 3 L. Yu, Q. Zhu, S. Song, B. McElhenny, D. Wang, C. Wu, Z. Qin, J. Bao, Y. Yu, S. Chen and Z. Ren, *Nat. Commun.*, 2019, **10**, 5106.
- 4 F. Song, M. M. Busch, B. Lassalle-Kaiser, C. S. Hsu, E. Petkucheva, M. Bensimon, H. M. Chen, C. Corminboeuf and X. Hu, *ACS Cent. Sci.*, 2019, **5**, 558–568.